

# Weekly-gridded Aquarius L-band radiometer/scatterometer observations and salinity retrievals over the polar regions: applications for cryospheric studies

L. Brucker<sup>1,2</sup>, E. Dinnat<sup>1,3</sup>, and L. S. Koenig<sup>1</sup>

<sup>1</sup>NASA GSFC, Cryospheric Sciences Laboratory, Code 615, Greenbelt, 20771 MD, USA

<sup>2</sup>Goddard Earth Sciences Technology and Research Studies and Investigations, Universities Space Research Association, Columbia, MD 21044, USA

<sup>3</sup>Chapman University, Orange, CA, USA

Received: 25 November 2013 – Accepted: 28 November 2013

– Published: 12 December 2013

Correspondence to: L. Brucker (ludovic.brucker@nasa.gov)

Published by Copernicus Publications on behalf of the European Geosciences Union.

Title Page

Abstract

Introduction

Conclusions

References

Tables

Figures

⏪

⏩

◀

▶

Back

Close

Full Screen / Esc

Printer-friendly Version

Interactive Discussion

## Abstract

Passive and active observations at L band (frequency  $\sim 1.413$  GHz) from the Aquarius/SAC-D mission offer new capabilities to study the polar regions. However, due to the lack of polar-gridded products, applications over the cryosphere are limited.

To allow for an efficient use of the Aquarius data over the polar regions, and to move forward our understanding of the L-band observations of ice sheet, sea ice, permafrost, and polar oceans, we present three weekly-polar-gridded products. Aquarius data at latitudes higher than  $50^\circ$  were averaged and gridded into three weekly products of Brightness Temperature (TB), Normalized Radar Cross Section (NRCS), and Sea Surface Salinity (SSS). These products are suited for cryospheric studies, and each grid cell contains sea ice fraction and the standard deviation of TB, NRCS, and SSS along with the number of footprint observations collected during the seven-day cycle. The data sets are produced on the version 2.0 Equal-Area Scalable Earth (EASE2.0) grid, with a grid cell resolution of 36 km. This paper describes the products, and presents maps and time series of Aquarius weekly-gridded data over the Greenland and Antarctic ice sheets, sea ice in both hemispheres, subarctic land where seasonal snow and frozen soil may exist, and the polar oceans. A brief analysis of L-band observations is given to encourage future use of the products. They can be used for improving our understanding of low microwave frequency observations, and for the development of algorithms. The new weekly-polar-gridded datasets start in August 2011, with the first Aquarius observations, and it is anticipated that they will be updated on a monthly basis following the release schedule of the Level 2 data sets.

## 1 Introduction

The cryosphere has been extensively studied using passive microwave satellite observations for over four decades. The first imaging radiometer, the Electrically Scanning Microwave Radiometer, launched in 1972 provided the earliest maps of the global sea

TCD

7, 5921–5970, 2013

### Aquarius weekly-gridded products to monitor the polar regions

L. Brucker et al.

Title Page

Abstract

Introduction

Conclusions

References

Tables

Figures

⏪

⏩

◀

▶

Back

Close

Full Screen / Esc

Printer-friendly Version

Interactive Discussion



## Aquarius weekly-gridded products to monitor the polar regions

L. Brucker et al.

Title Page

Abstract

Introduction

Conclusions

References

Tables

Figures

⏪

⏩

◀

▶

Back

Close

Full Screen / Esc

Printer-friendly Version

Interactive Discussion

ice cover (Zwally et al., 1983). In 1978, the longest continuous passive microwave data record started with the launch of the Scanning Multichannel Microwave Radiometer (SMMR). This data record, used for example to monitor sea-ice cover properties, ice sheet melt, and snow on land, continues to the present with the series of Special Sensor Microwave Imager Sounder (SSM/I, SSMIS), and Advanced Microwave Scanning Radiometers (AMSR-E, AMSR2). The lowest frequency observations available at high latitudes were available at  $\sim 7$  GHz with SMMR and the AMSRs (and only at 18 GHz with the SSM/Is).

In the 1970s, observations at 1.4 GHz were collected by the Skylab S-194 radiometer (Jackson et al., 2004), however the orbit characteristics did not enable the monitoring of the polar regions. Since late 2009, passive L-band observations from the Soil Moisture and Ocean Salinity (SMOS) mission are routinely collected over both polar regions. In addition, the Aquarius/SAC-D mission provides both passive and active L-band observations since August 2011. Similar observations will be collected with the forthcoming Soil Moisture Active/Passive (SMAP) mission (whose launch is currently planned for late 2014). Despite the fact that these missions have been primarily designed for the monitoring of either Sea Surface Salinity (SSS) or soil moisture, new applications are being developed to study the cryosphere.

In the microwave domain, dry snow and ice are low-loss media and the radiation penetrates into the snow/ice cover. Penetration of microwaves is inversely proportional to losses due to scattering and absorption, and thus increases as frequency decreases. L-band dry snow and ice dielectric losses are very small (e.g., Mätzler, 1987; Warren et al., 2008), and the L-band radiation likely emanates from one to two orders of magnitude deeper than the radiation observed at 6.9 GHz (Surdyk, 2002). Thus, the L-band radiation can emanate from hundreds to thousands of meters deep (i.e. centuries old ice over the Antarctic plateau for example), which opens new research topics and motivates the development of innovative approaches to study long-term climatic changes over the ice sheets. Moreover, specific regions of the Antarctic ice sheet can be used as calibration and validation sites for L-band radiometers (e.g., Drinkwater



over different time scales (e.g. daily, weekly, monthly, and seasonal time scales) (Wentz and Le Vine, 2012; Le Vine et al., 2012). Therefore, the Aquarius products available do not include weekly-gridded data sets of TB and NRCS appropriate for studying the Earth's polar regions and the cryosphere. Moreover, the Level 3 SSS products use a projection that is not optimal for studying the high latitudes.

To allow for an efficient use of the Aquarius data over the polar regions, and to move forward our understanding of the L-band observations of ice sheet, sea ice, permafrost, and polar oceans, we present in this manuscript three weekly-polar-gridded products of TB, NRCS, and SSS. These products also include sea ice fraction (ICEF). The gridded products were produced on the version 2.0 Equal-Area Scalable Earth (EASE) grid (Brodzik et al., 2012). Each grid cell is 36km × 36km. This grid and resolution were selected because they offer a fair compromise between Aquarius' high sampling along track (an observation every 10 km) and the distance between tracks, and they will be used by SMAP. Gridded data were produced using all the valid Aquarius observations from the seven-day satellite cycle.

We describe the Aquarius radiometers and scatterometer in Sect. 2 along with the criteria for valid data. In Sect. 3, we introduce the details of the Aquarius weekly-polar-gridded products. We present the weekly-polar-gridded maps resulting of the TB and NRCS products in Sects. 4 and 5, respectively, with a focus on the Greenland and Antarctic ice sheets, and sea ice in both hemispheres. In Sects. 6 and 7, we present data over land where seasonal snow and frozen soil exist, and maps of polar ocean salinities to discuss the effect of sea ice contamination.

Weekly-polar-gridded products presented in this paper are available on the NASA Cryosphere Science Research Portal <http://neptune.gsfc.nasa.gov/csb/index.php?section=273>. They cover the entire Aquarius mission period since its start in August 2011. It is anticipated that the products will be updated on a monthly basis following the release schedule of the Level 2 data sets by PO.DAAC.

**Aquarius  
weekly-gridded  
products to monitor  
the polar regions**

L. Brucker et al.

Title Page

Abstract

Introduction

Conclusions

References

Tables

Figures



Back

Close

Full Screen / Esc

Printer-friendly Version

Interactive Discussion



## 2 Aquarius data

The passive Aquarius instruments consist of three radiometers providing TB at 1.413 GHz in V and H polarizations. The third Stokes parameter is also measured, but assumed null at the surface. Observations of the third Stokes parameter are used to retrieve properties of the Faraday rotation in the ionosphere (Yueh, 2000), and the antenna cross-polarization coupling (Le Vine et al., 2011; Kim et al., 2011). The three radiometers (1, 2, and 3, at the incidence angles of 28.7°, 37.8°, and 45.6°, respectively) are in a push-broom alignment (i.e. non-scanning) pointing to the right-hand side of the orbit. Most of the time, they point to the night side of the sun-synchronous orbit, but solar contamination in the main beams is possible at high latitudes seasonally (Dinnat and Le Vine, 2008). Other radiometers used to the study of the cryosphere typically operate at incidence angles of 53–55°, closer to the Brewster angle for the snow/air interface. The lower Aquarius incidence angles imply that observations are more sensitive to the snow/air interface, and surface snow metamorphism (Brucker et al., 2013b).

Table 1 provides the radiometers' footprint dimensions, which are increasing as the incidence angle increases. The spacecraft orbits with a seven-day repeat cycle. These characteristics, and the fact that the radiometers are in a push-broom alignment, imply that the spatial coverage becomes sparser as latitude decreases. According to the orbit inclination and the different radiometers' incidence angles, the areas unobserved at the poles differ for each sensor and hemisphere (Table 1). In the Northern Hemisphere (NH), the largest coverage is obtained using beam 3, whereas in the Southern Hemisphere (SH) beam 3 has the smallest coverage.

As mentioned previously, the accuracy and stability of Aquarius radiometric observations is remarkably good. The radiometer NEDT is 0.15 K, and observations have shown stability within  $\pm 0.2$  K over the ocean and celestial Sky over several months (Dinnat et al., 2013; Lagerloef et al., 2013).



## Aquarius weekly-gridded products to monitor the polar regions

L. Brucker et al.

Title Page

Abstract

Introduction

Conclusions

References

Tables

Figures

⏪

⏩

◀

▶

Back

Close

Full Screen / Esc

Printer-friendly Version

Interactive Discussion

Aquarius Level 2 product (version 2.0, September 2013) consists of the footprint observations and retrievals along track (i.e. the swath data). It also consists of ancillary data, flags, converted telemetry, and navigation data. One example of ancillary data is the ICEF. This variable is not retrieved with the satellite observations. The ICEF results from a combination of two elements: simulated sea ice concentration, and antenna characteristics. Sea ice concentration is simulated by the US National Centers for Environmental Prediction (NCEP), and distributed as the Global Forecast System (GFS) Global Data Assimilation System (GDAS) sea ice product. Aquarius sea ice fraction is thus simulated, and differs from the passive microwave satellite sea ice concentration products (e.g., Comiso et al., 2003). Hereafter, the use of ICEF refers to the simulated sea ice concentration integrated over the sensor's field of view and weighted by the antenna gain patterns. Similarly, land fraction data is integrated over the sensor's field of view and weighted by the antenna gain patterns (Dinnat and Le Vine, 2007; Le Vine et al., 2011).

Level 2 TB product is computed after empirical calibration of the measured antenna temperatures against a forward radiative transfer model. The antenna temperatures are then corrected for the emission of extraterrestrial sources (Sun, Moon, celestial Sky), the effect of the integration over the antenna gain patterns, the Faraday rotation, and atmospheric effects. This provides the TBs at the Earth's surface. Over the oceans, the TB is corrected for the effects of surface roughness using the scatterometer observations, and a simulated wind speed. The remaining TB for a smooth surface is converted into SSS using ancillary data for the sea surface temperature, and a model for the sea water dielectric constant. Details can be found in Wentz and Le Vine (2012); Le Vine et al. (2012) and Piepmeier et al. (2013). We use these Aquarius Level 2 data to produce weekly-gridded products of TB (at V and H polarizations), NRCS (at VV, VH, and HH polarizations), SSS, and ICEF.

### 3 Weekly-polar-gridded product details

A gridded product has three main characteristics: projection, spatial resolution, and temporal resolution. These characteristics were defined according to the satellite observations, and to ensure consistency with the forthcoming SMAP mission. The EASE2.0 grid (Brodzik et al., 2012) was chosen, and the grid cell spatial resolution set to 36 km × 36 km. These characteristics are appropriate for the Aquarius observations at latitudes higher than 50°. At these high latitudes, there are limited areas not observed. Therefore, the trade-off between spatial resolution and data coverage is fair. Since Aquarius observations are, however, recorded every 10 km along track, it is possible for specific applications to grid the data with a refined spatial resolution better than 36 km. The temporal resolution of the gridded product was defined by the time of revisit: seven days.

Gridded data were produced using all the Aquarius observations deemed as RFI free, and recorded during nominal operation of the spacecraft. Non-nominal operation dates include maneuvers and anomaly periods.

For TB, each radiometer was treated independently to produce three weekly-gridded TB products corresponding to observations from the ascending orbit, the descending orbit, and both orbit types combined. The distinction per beam is necessary due to the different incidence angles, which lead to different reflection intensities at the interface created by dielectric constant changes (e.g. snow/air interface) (Brucker et al., 2013b). For each seven-day cycle, all observations from a given radiometer (RFI free and recorded during nominal operation) whose footprint center was within a given 36 km grid cell were averaged together, and the standard deviation was calculated.

For NRCS, each beam and each orbit type was treated independently. The distinction for each beam is also needed due to the different incidence angles. The distinction between each orbit type is necessary because of the anisotropy of the ice covered surfaces (addressed in Sect. 5.1).

## Aquarius weekly-gridded products to monitor the polar regions

L. Brucker et al.

Title Page

Abstract

Introduction

Conclusions

References

Tables

Figures



Back

Close

Full Screen / Esc

Printer-friendly Version

Interactive Discussion

## Aquarius weekly-gridded products to monitor the polar regions

L. Brucker et al.

Title Page

Abstract

Introduction

Conclusions

References

Tables

Figures

⏪

⏩

◀

▶

Back

Close

Full Screen / Esc

Printer-friendly Version

Interactive Discussion

For SSS, two weekly-gridded products are available. The first product provides the SSS corresponding to the weekly-gridded TB: data are distributed separated per beam and per orbit type, and include combined ascending and descending orbits. The second product was generated combining the SSS retrieved from the three beams and both orbit types. In the latter case, the weekly-gridded SSS values are calculated using the maximum amount of retrievals.

SSS retrievals where the radiometer land fraction was  $\geq 0.25$  were not considered. If left uncorrected, a land fraction of as little as 0.001 can be detrimental to the SSS retrieval ( $\sim 0.2$ – $0.4$  psu error; Dinnat and Le Vine, 2007). However, there is a first order correction for the effect of land contamination in the Level 2 SSS retrieval that should remove most of the error (Sect. 3.8; Wentz and Le Vine, 2012). In addition, the level of acceptable residual error in coastal studies will depend on specific applications of the product. For these reasons, we set a relatively high threshold for land contamination. Because we provide the information on the land fraction for each grid cell, the user has the opportunity to select a more stringent threshold when needed.

TB, NRCS, and SSS weekly averages are provided in conjunction with the standard deviations of all footprint observations/retrievals with the given grid cell. Of note, the statistical significance of the standard deviation has to be evaluated against the number of footprint observations (NFP) in the grid cell.

Grid cells without data can result from missing observations either because the cells fall in between beam tracks (permanently missing), or because all data gathered were deemed invalid for a given time period. In these situations, a linear interpolation of the weekly-gridded TB and NRCS was applied in grid cells without observations during the cycle. To avoid interpolating over too large a region in case of significant data loss, the interpolation was not applied (and a NaN element is provided) where six or more contiguous grid cells had no data. Note that because each product contains the number of footprint observations per grid cell, it is easy to identify interpolated values where the number of observations per grid cell is 0. This allows users to either disregard the interpolated data, or apply another interpolation method best suited for their studies.

In any case, one must be cautious with the use of interpolated data, even though the Aquarius radiometer field of views are larger than the 36 km grid cell resolution.

The TB, NRCS, and SSS products are processed for every Aquarius cycle, and distributed in HDF5 format at <http://neptune.gsfc.nasa.gov/csb/index.php?section=273>.

Future release dates depend on the release of the Level 2 product, which are currently released monthly in a one month batch. We also provide ancillary files containing the grid cell center latitude and longitude, and the grid cell mean land fraction, as well as a look-up table to convert date to orbit cycle number. Table 3 summarizes the data distributed in each of the three products.

### 3.1 Aquarius 36 km weekly-polar-gridded TB, and SSS

This product containing TB, SSS, and ICEF is composed of six files per cycle: one per beam, and one per hemisphere. Each file contains the weekly-gridded TB, SSS, and ICEF of the ascending orbits, descending orbits, and the two orbit types combined. The data sets consist of weekly mean TB V, TB H, and SSS, along with the standard deviations within the grid cell (TBV\_STD, TBH\_STD, and SSS\_STD). This product also contains the radiometer ice fraction (ICEF\_RAD and ICEF\_STD\_RAD for the mean and standard deviation, respectively). Standard deviation values are never interpolated.

### 3.2 Aquarius 36 km weekly-polar-gridded NRCS

This product containing NRCS and ICEF is composed of six files per cycle: one per beam, and one per hemisphere. Each file contains the weekly-gridded data of the ascending and descending orbits. NRCS observations from ascending and descending orbits were not combined together due to the anisotropy of the ice covered surfaces. The data consist of weekly mean NRCS at three polarizations (NRCS\_VV, NRCS\_VH, and NRCS\_HH), along with the standard deviations within the grid cell (NRCS\_VV\_STD, NRCS\_VH\_STD, and NRCS\_HH\_STD). This product also contains

## Aquarius weekly-gridded products to monitor the polar regions

L. Brucker et al.

Title Page

Abstract

Introduction

Conclusions

References

Tables

Figures

⏪

⏩

◀

▶

Back

Close

Full Screen / Esc

Printer-friendly Version

Interactive Discussion

the scatterometer ice fraction (ICEF\_SCA and ICEF\_STD\_SCA for the mean and standard deviation, respectively).

### 3.3 Aquarius 36 km weekly-polar-gridded SSS3b

This product combines SSS retrievals from all three beams, as retrievals of SSS should be independent of the beam (i.e. of the incidence angle). However, the error on SSS retrievals could vary slightly with the beam as the outer beam averages over a larger field of view and is more sensitive to surface roughness (in horizontal polarization) for example. This product is composed of two files per cycle: one per hemisphere. Each file contains the weekly-gridded SSS of the ascending orbit, descending orbit, and the two orbit types combined, along with the standard deviation within the grid cell (SSS\_STD). The distinction between the two orbit types is needed since differences have been identified (Lagerloef et al., 2013).

## 4 L-band TB product analysis over the ice sheets

Microwave observations are sensitive to snow properties (e.g. liquid water, grain size, density, temperature) (Ulaby et al., 1986; Mätzler, 1987) and to their vertical variations (Brucker et al., 2010, 2011). This sensitivity to snow properties has been used to monitor various geophysical properties over the ice sheets, such as snow melt extent (e.g., Torinesi et al., 2003; Tedesco et al., 2007), snow accumulation (e.g., Abdalati and Steffen, 1998; Winebrenner et al., 2001), and grain size (Brucker et al., 2010; Picard et al., 2012). This section aims at providing for the first time an overall presentation of the Aquarius weekly-polar-gridded TB over the Greenland Ice Sheet (GIS) and Antarctic Ice Sheet (AIS). It is beyond the scope of this study to address the specifics in the data, and to relate quantitatively the remote sensing observations to geophysical properties. The products presented here enable these in-depth analyses for future research.

## Aquarius weekly-gridded products to monitor the polar regions

L. Brucker et al.

Title Page

Abstract

Introduction

Conclusions

References

Tables

Figures

⏪

⏩

◀

▶

Back

Close

Full Screen / Esc

Printer-friendly Version

Interactive Discussion



## Aquarius weekly-gridded products to monitor the polar regions

L. Brucker et al.

Title Page

Abstract

Introduction

Conclusions

References

Tables

Figures

⏪

⏩

◀

▶

Back

Close

Full Screen / Esc

Printer-friendly Version

Interactive Discussion

The GIS and AIS have craggy coastal regions, mountainous areas, and thus present steep slopes in their peripheries, and multiple surface types in the grid cells. Ice sheet roughness is controlled by bedrock topography, and by snow accumulation, erosion, and redistribution (Furukawa and Young, 1997; Long and Drinkwater, 2000). Topographic variations within the Aquarius 3-dB footprint contribute to the L-band observations, and could, therefore impact the retrievals of geophysical properties; evidences have been identified over North Africa and Australia (Utku and Le Vine, 2013). The interpretation of the L-band observations should thus be made with caution in areas with strong elevation change and heterogeneity.

### 4.1 The Greenland ice sheet

Interesting spatial and temporal variations are revealed by maps of L-band TB observations over the GIS (Fig. 2). Overall, TBs are high ( $> 250$  K) year round in the northern coastal regions (extending up to  $\sim 200$  km in land). Whereas the other coastal regions show a seasonal cycle with lower TBs in summer than in winter. This cycle directly results from the sea-ice seasonal cycle, and the presence of open water in summer. In North and northeast Greenland, sea ice is present year round, whereas it is not on the other Greenlandic coasts (see ice concentration maps in Brucker et al., 2013a).

Farther inland, TBs increase from  $\sim 190$  K to  $\sim 230$  K as elevation increases, and therefore as temperature, snow accumulation, and days of melting snow decrease. The lowest TBs ( $\sim 180$  K) are found in the central part of south Greenland at latitudes between  $\sim 62^\circ$  N and  $\sim 68^\circ$  N. Additionally, at these latitudes there is a clear distinction between the eastern and western sides of the GIS, with systematically lower TBs on the eastern side. This difference comes from the different ice sheet properties. South-east Greenland has the highest snow accumulation (Burgess et al., 2010), whereas southwest Greenland has lower snow accumulation and more melt; a large part of this latter region is in the ablation zone. Therefore, the L-band radiation emanates mainly from ice/firn/snow in southeast Greenland, and from ice/snow in southwest Greenland.



ing microwave TB (Magand et al., 2008), Fig. 4 shows that similar bias can be expected using L-band observations.

## 4.2 The Antarctic ice sheet

Low TBs (< 200 K) observed in January and February in the continent periphery are due to the presence of the surrounding sea-ice-free ocean (Fig. 5). This effect is only visible on a narrow band of latitudes. Slightly farther inland, there is another narrow band of latitudes with very high TBs (250–265 K) year round. The spatial extent of these high TBs progresses inland as snow is melting, and reaches its maximum in January.

The lowest TBs not contaminated by sea-ice-free ocean are located on the high elevation domes of the Antarctic Plateau (eastern part of the continent). The lowest mean-annual TBs of the Plateau are located at both polarizations in grid cells within or adjacent to the Vostok Lake (76.396° S, 105.852° E). This suggest that the radiometrically cold lake and/or the particular ice properties over the lake influence the L-band observations. There is also an obvious contrast between the Antarctic Plateau, and the West AIS (WAIS). The Plateau has higher elevations, lower snow accumulations, no melt events, and thus lower TB than Mary Byrd Land (Fig. 5). Several previous studies discuss these spatial distributions of microwave observations at higher frequencies and their correlation with geophysical properties (e.g., Long and Drinkwater, 2000; Schneider and Steig, 2002; Schneider et al., 2004; Picard et al., 2009; Brucker et al., 2010), which are also evident at L band.

Strong and direct interactions between ice sheet and ocean occur under ice shelves. The Amery ice shelf and ice shelves in the Peninsula (e.g. Larsen C located 67.5° S, 62.5° W) are characterized by low winter TBs (Fig. 5). This suggests that Aquarius observations could be analyzed in these regions to study the relationship between L-band TBs and ice shelf properties (e.g. thickness). Future studies could also investigate the different processes that can operate at the ice-shelf base (e.g. refreezing, or melting releasing fresher water initiating deep water formation).

### Aquarius weekly-gridded products to monitor the polar regions

L. Brucker et al.

Title Page

Abstract

Introduction

Conclusions

References

Tables

Figures

⏪

⏩

◀

▶

Back

Close

Full Screen / Esc

Printer-friendly Version

Interactive Discussion



## Aquarius weekly-gridded products to monitor the polar regions

L. Brucker et al.

Title Page

Abstract

Introduction

Conclusions

References

Tables

Figures

⏪

⏩

◀

▶

Back

Close

Full Screen / Esc

Printer-friendly Version

Interactive Discussion

Considering one weekly-gridded TB data set in winter (July) and in summer (January), the ranges of TB for the whole observed AIS are 206–270 K and 178–250 K at V and H polarizations, respectively (Fig. 6). At both polarizations, the range of TB is smaller than that observed over the GIS. Distributions slightly change between the two seasons, with more grid cells having higher TBs in summer, but the ranges do not vary much. As noted earlier, the lowest summer TBs are due to the presence of open water along the coast.

The Antarctic ice sheet can be used as a target for sensor calibration and intercalibration at L band. Dome C is a potential candidate (Drinkwater et al., 2004; Macelloni et al., 2013). Over the period September 2011–September 2013, the mean TBs observed by Aquarius' radiometer 1 at Dome C (75.1° S, 123.35° E, snow accumulation rates of 7.2 cm yr<sup>-1</sup> (Urbini et al., 2008)) are 202.53 ± 0.26 K, and 190.12 ± 0.47 K at V and H polarization, respectively (Fig. 7). These TB standard deviations over the two-year period are low, but they are higher than the radiometers' sensitivity of 0.15 K. Over the WAIS, in one grid cell of the Mary Byrd region (79.242° S, 117.718° W), mean TBs for the same period are 229.68 ± 0.56 K and 222.12 ± 0.74 K at V and H polarization, respectively (Fig. 7). Temporal variability is higher at H than V polarization, which was already observed at L band (Macelloni et al., 2013; Brucker et al., 2013b), and at higher microwave frequencies (e.g., Lacroix et al., 2009; Brucker et al., 2011).

Aquarius provides the lowest microwave frequency observations to routinely observe the cryosphere. The next lowest frequencies are available on AMSR2 in the frequency range 6.9–89 GHz. Observations from these sensors at Dome C are presented for an entire year in a scatter plot of TB H as a function of TB V (Fig. 8). The amplitude of the variation during the year decreases as frequency decreases (i.e. the width of the ellipse is reduced going from 89 GHz (gray) to 6.9 GHz (red)). This is explained by the lower frequency channels having larger penetration depths, and being thus less sensitive to variations in the temperature profile resulting from solar heating. Considering data from AMSR2 only, values at V polarization increase as frequency decreases (from gray to red), but values at H polarization decrease as frequency decreases (i.e. each

ellipse of AMSR2 TB observations move toward the bottom right corner of Fig. 8 as frequency decreases). TBs observed by each Aquarius' radiometer decrease as the incidence angle increases (from radiometer 1 to 3; Fig. 8). Aquarius TB V observations are higher than every annual mean AMSR2 TB V. However, Aquarius TB H observations are higher than any of the annual mean AMSR2 TB H. Aquarius radiometers operate at lower incidence angles than AMSR2 ( $< 45.6^\circ$  vs.  $55^\circ$ ), which likely explains most of the difference. Modeling studies are required to quantify the contributions of the different incidence angles.

### 4.3 Sea ice

In contrast to ice sheet, sea ice is a more dynamic cover. Sea ice forms, grows, and melts according to the seasons, and some sea ice remains year round in certain regions of both the Arctic and Antarctic. Microwave TB observations depend on the physical properties of sea ice and its overlying snow cover, both of which evolve with time. They also depend on large scale properties of the sea ice cover, whether the sea ice cover is packed or fractured with the presence of leads (open water or new/thin ice).

To present Aquarius weekly-polar-gridded TB product over sea ice, all data associated with the presence of sea ice is used. This implies that extensive areas with low TBs are also considered (Figs. 9 and 10). For reference, TB V of ice-free ocean is typically less than 125 K for radiometer 3, and less than 107 K for radiometer 1. TBs higher than that are observed with a presence of sea ice.

In the NH (Fig. 9), TBs are the highest when snow on sea ice is melting (typically in May and June). TBs are lower during the summer months likely when the sea ice cover is more fractured, with leads exposing open sea water. Overall, a similar TB evolution occurs during the year over the SH sea ice cover (Fig. 10). In Fig. 10, the Ross polynia ( $75^\circ$  S,  $178^\circ$  E) can be observed in Summer (January–March).

Sea ice can extend to low latitudes (especially in the SH down to latitudes of  $\sim 55^\circ$  S or less). There, Aquarius spatial coverage is significantly reduced. At higher latitudes, where more observations are available, some noise is visible on the weekly TB maps

**Aquarius  
weekly-gridded  
products to monitor  
the polar regions**

L. Brucker et al.

Title Page

Abstract

Introduction

Conclusions

References

Tables

Figures

⏪

⏩

◀

▶

Back

Close

Full Screen / Esc

Printer-friendly Version

Interactive Discussion



(e.g. distinct lines in July; Fig. 9). This is related to the fast changing properties of the sea ice cover during the one-week period used to create the gridded product.

To analyze further Aquarius TBs over sea ice, the relationship between ICEF and TB V is analyzed. To that end, swath TBs and ICEFs were used, so that there is no influence of gridding and averaging. Moreover, data in the Ross Sea were used to avoid land contamination. Figure 11 illustrates two important and distinct points. First, it shows the high sensitivity of TB to the presence of sea ice; there is a continuous increase of TB V (radiometer 1) between  $\sim 100$  K, the level for ice-free water, and  $\sim 250$  K which corresponds to a packed Antarctic sea ice cover in winter. Second, Fig. 11 shows that there are numerous low TB observations ( $< 107$  K) associated with ICEFs ranging from 0 to 0.5. From our investigations, we noticed that an ICEF of 0.5 raises TB about 70 K (85 K) above the nominal ocean TB level at V (H) polarization using radiometer 1. ICEF comes from simulated sea ice concentration integrated over the sensor's field of view and weighted by the antenna gain patterns. It is very likely that, for the data with a surprisingly low TB, the NCEP GSF GDAS sea ice concentration overestimated the presence of ice.

Studies carried out with SMOS observations show that the L-band TB contains information about thin sea ice thickness (Kaleschke et al., 2010; Huntemann et al., 2013). Since thin ice is fragile it is associated with a very heterogeneous surface. The Aquarius large footprint observations will make the retrievals of thin sea ice thickness very challenging. Though, they may be complementary to CryoSat-2 sea ice thickness as for instance retrieved by Hendricks et al. (2013).

## 5 Active microwave product analysis

While space-borne L-band synthetic aperture radar (SAR) observations were available from Advanced Land Observing Satellite (ALOS) PALSAR, space-borne L-band scatterometer observations were first collected by Aquarius. NRCS analysis over the ice sheets was previously studied at C- and Ku-band (Massom and Lubin, 2006, and

### Aquarius weekly-gridded products to monitor the polar regions

L. Brucker et al.

Title Page

Abstract

Introduction

Conclusions

References

Tables

Figures

⏪

⏩

◀

▶

Back

Close

Full Screen / Esc

Printer-friendly Version

Interactive Discussion



references in there). In this section, NRCS observations are presented at the three different polarizations (VV, VH, and HH) that could be used to infer snow/ice and surface properties over ice sheets, and sea ice.

## 5.1 Ice sheets

5 Over the GIS, there is a full spatial coverage of the northern portion of the ice sheet (latitudes higher than 77° N). As with the radiometer (see Sect. 2 and Fig. 1), the amount of valid data considered in this weekly-gridded product is lower for the descending orbits than the ascending orbits due to the RFI contamination.

10 The different polarizations contain information on the structural characteristics of the ice/firn/snow medium and its surface. NRCS values recorded during the first week of January 2013 over the GIS show similar patterns at the three polarizations (Fig. 12, first row), and similar patterns between the ascending and descending orbit observations (Fig. 12, first row vs. second row), though small differences in intensity exist. At higher frequencies, the spatial distribution of NRCS was correlated with the wet snow zone, the percolation zone, and the dry snow zone (Long and Drinkwater, 1994). Seasonal variations are observed on the NRCS, but they are small. Long and Drinkwater (1999) provide a detailed analysis of the spatial and temporal variations of the NRCS over the different zones of the GIS using Ku-band observations, and the relationship with snow properties. Similar processes may be related to the L-band NRCS observations.

20 Over the AIS (Fig. 13), the main patterns are also similar at all three polarizations. However, NRCS recorded during ascending and descending orbits are significantly different. Differences between orbit types are visible across the ice sheet, but predominantly in East Antarctica. For instance, differences are easily identified in the Dronning Maud Land sector (20° W–45° E), in the Victoria Land sector (140° E–160° E), and in between (e.g. 75° E–105° E). The linear correlation coefficient between NRCS VV observations of the ascending and descending orbits for this first week of July 2013 is 0.52, which illustrates the importance of distinguishing the ascending and descending orbits when analyzing the NRCS observations. At the three polarizations, NRCS obser-

### Aquarius weekly-gridded products to monitor the polar regions

L. Brucker et al.

Title Page

Abstract

Introduction

Conclusions

References

Tables

Figures

⏪

⏩

◀

▶

Back

Close

Full Screen / Esc

Printer-friendly Version

Interactive Discussion









plied. Interpolated values can be tracked by the users using the number of footprint observations. The three products are available in HDF5 format starting from late August 2011. It is anticipated that they will be updated on a monthly basis following the release schedule of the Level 2 data sets.

L-band observations are sensitive to RFI. Their presence is localized mostly in the NH, and substantially impacts the monitoring of continental land, the GIS, and the Beaufort sea. The magnitude of the RFI contribution depends on the orbit (ascending vs. descending). Over the GIS, observations collected during the ascending orbits are significantly less impacted by RFI.

Due to the anisotropy of the ice-covered surface, NRCS observations recorded during the ascending and descending orbits must be studied separately. Substantial difference exists over sea ice and the AIS.

These products enhance the use of combined passive and active L-band observations to study the cryosphere. The spatial distributions of Aquarius TB and NRCS over the Greenland and Antarctic ice sheet were presented. We showed that the 2012 melt event over the GIS highest elevations impacted the L-band TB, with implications for surface mass balance monitoring. NRCS values over Antarctic sea ice shows a transition (“bright NRCS ring”) from the packed sea ice to lower ICEF of 0.3–0.4. We also showed that both active and passive observations over land present distinct values in summer and winter, depending on the soil physical state. Aquarius 3-dB footprints are large and make the monitoring of sea ice complex. In both hemispheres, TB over sea ice was the highest when snow on sea ice melts, and the lowest in summer. Studying the surface ocean freshening resulting from ice sheet or sea ice melting is challenging. The sensitivity of the Aquarius SSS retrievals is degraded in cold waters, with sea ice and icebergs in the field of view, and over rough oceans.

The products described in this manuscript are available on the NASA Cryosphere Science Research Portal <http://neptune.gsfc.nasa.gov/csb/index.php?section=273> in HDF5 format for improving our understanding of low microwave frequency observa-

**Aquarius  
weekly-gridded  
products to monitor  
the polar regions**

L. Brucker et al.

Title Page

Abstract

Introduction

Conclusions

References

Tables

Figures



Back

Close

Full Screen / Esc

Printer-friendly Version

Interactive Discussion





---

**Aquarius  
weekly-gridded  
products to monitor  
the polar regions**

L. Brucker et al.

[Title Page](#)[Abstract](#)[Introduction](#)[Conclusions](#)[References](#)[Tables](#)[Figures](#)[⏪](#)[⏩](#)[◀](#)[▶](#)[Back](#)[Close](#)[Full Screen / Esc](#)[Printer-friendly Version](#)[Interactive Discussion](#)

Brucker, L., Dinnat, E., Picard, G., and Champollion, N.: Effect of snow surface metamorphism on Aquarius L-band radiometer observations at Dome C, Antarctica, IEEE T. Geosci Remote, TGRS-2013-01172, submitted, 2013b. 5926, 5929, 5936

Burgess, E. W., Forster, R. R., Box, J. E., Mosley-Thompson, E., Bromwich, D. H., Bales, R. C., and Smith, L. C.: A spatially calibrated model of annual accumulation rate on the Greenland Ice Sheet (1958–2007), J. Geophys. Res.-Earth, 115, F02004, doi:10.1029/2009JF001293, 2010. 5933, 5934

Comiso, J. C., Cavalieri, D. J., and Markus, T.: Sea ice concentration, ice temperature, and snow depth using AMSR-E data, IEEE T. Geosci Remote, 41, 243–252, doi:10.1109/TGRS.2002.808317, 2003. 5928

Dinnat, E. P. and Le Vine, D. M.: Effects of the antenna aperture on remote sensing of sea surface salinity at L-band, IEEE T. Geosci. Remote, 45, 2051–2060, doi:10.1109/TGRS.2007.890807, 2007. 5928, 5930

Dinnat, E. P. and Le Vine, D. M.: Impact of sun glint on salinity remote sensing: an example with the aquarius radiometer, IEEE T. Geosci. Remote, 46, 3137–3150, doi:10.1109/TGRS.2008.2000629, 2008. 5926

Dinnat, E., Le Vine, D., and Abraham, S.: Aquarius Cold Sky maneuvers: assessing calibration bias, temporal drift, and antenna back lobes, IGARSS 2013, oral presentation, 2013. 5926

Drinkwater, M. R., Floury, N., and Tedesco, M.: L-band ice sheet brightness temperatures at Dome C, Antarctica: spectral emission modelling, temporal stability and impact of the ionosphere., Ann. Glaciol., 39, 391–396, doi:10.3189/172756404781814014, 2004. 5923, 5936

Entekhabi, D., Njoku, E., O'Neill, P., Kellogg, K., Crow, W., Edelstein, W., Entin, J., Goodman, S., Jackson, T., Johnson, J., Kimball, J., Piepmeier, J., Koster, R., Martin, N., McDonald, K., Moghaddam, M., Moran, S., Reichle, R., Shi, J.-C., Spencer, M., Thurman, S., Tsang, L., and Van Zyl, J.: The Soil Moisture Active Passive (SMAP) mission, P. IEEE, 98, 704–716, doi:10.1109/JPROC.2010.2043918, 2010. 5924

Furukawa, T. and Young, N. W.: Comparison of microwave backscatter measurements with observed roughness of the snow surface in East Queen Maud Land, Antarctica, in: Third ERS Symposium on Space at the service of our Environment, edited by: Guyenne, T.-D. and Danesy, D., vol. 414 of ESA Special Publication, 803 pp., 1997. 5933

## Aquarius weekly-gridded products to monitor the polar regions

L. Brucker et al.

Title Page

Abstract

Introduction

Conclusions

References

Tables

Figures

◀

▶

◀

▶

Back

Close

Full Screen / Esc

Printer-friendly Version

Interactive Discussion



- Hall, D. K., Comiso, J. C., DiGirolamo, N. E., Shuman, C. A., Box, J. E., and Koenig, L. S.: Variability in the surface temperature and melt extent of the Greenland ice sheet from MODIS, *Geophys. Res. Lett.*, 40, 2114–2120, doi:10.1002/grl.50240, 2013. 5934
- Hendricks, S., Ricker, R., and Helm, V.: AWI CryoSat-2 Sea Ice Thickness Data Product, Tech. rep., Alfred Wegener Institute, meereis portal, Bremerhaven, Germany, 2013. 5938
- Huntemann, M., Heygster, G., Kaleschke, L., Krumpfen, T., Mäkynen, M., and Drusch, M.: Empirical sea ice thickness retrieval during the freeze up period from SMOS high incident angle observations, *The Cryosphere Discuss.*, 7, 4379–4405, doi:10.5194/tcd-7-4379-2013, 2013. 5938
- Jackson, T. J., Hsu, A. Y., van de Griend, A., and Eagleman, J. R.: Skylab L-band microwave radiometer observations of soil moisture revisited, *Int. J. Remote Sens.*, 25, 2585–2606, doi:10.1080/01431160310001647723, 2004. 5923
- Kaleschke, L., Maaß, N., Haas, C., Hendricks, S., Heygster, G., and Tonboe, R. T.: A sea-ice thickness retrieval model for 1.4 GHz radiometry and application to airborne measurements over low salinity sea-ice, *The Cryosphere*, 4, 583–592, doi:10.5194/tc-4-583-2010, 2010. 5924, 5938
- Kerr, Y., Waldteufel, P., Wigneron, J.-P., Delwart, S., Cabot, F., Boutin, J., Escorihuela, M.-J., Font, J., Reul, N., Gruhier, C., Juglea, S., Drinkwater, M., Hahne, A., Martin-Neira, M., and Mecklenburg, S.: The SMOS mission: new tool for monitoring key elements of the global water cycle, *P. IEEE*, 98, 666–687, doi:10.1109/JPROC.2010.2043032, 2010. 5924
- Kim, S.-B., Wentz, F., and Lagerloef, G. S. E.: Effects of antenna cross-polarization coupling on the brightness temperature retrieval at L-band, *IEEE T. Geosci Remote*, 49, 1637–1648, doi:10.1109/TGRS.2010.2087028, 2011. 5926
- Lacroix, P., Legresy, B., Remy, F., Blarel, F., Picard, G., and Brucker, L.: Rapid change of the snow surface properties at Vostok, East Antarctica, revealed by altimetry and radiometry, *Remote Sens. Environ.*, 113, 2633–2641, doi:10.1016/j.rse.2009.07.019, 2009. 5936
- Lagerloef, G., Kao, H.-Y., Meln, O., Hacker, P., Hackert, E., Chao, Y., Hilburn, K., Meissner, T., Yueh, S., Hong, L., and Lee, T.: Aquarius salinity validation analysis, Tech. rep., NASA, 2013. 5926, 5932, 5941
- Le Vine, D., Lagerloef, G. S. E., and Torrusio, S.: Aquarius and remote sensing of sea surface salinity from space, *P. IEEE*, 98, 688–703, doi:10.1109/JPROC.2010.2040550, 2010. 5924



## Aquarius weekly-gridded products to monitor the polar regions

L. Brucker et al.

Title Page

Abstract

Introduction

Conclusions

References

Tables

Figures

⏪

⏩

◀

▶

Back

Close

Full Screen / Esc

Printer-friendly Version

Interactive Discussion

- Picard, G., Brucker, L., Fily, M., Gallée, H., and Krinner, G.: Modeling time-series of microwave brightness temperature in Antarctica, *J. Glaciol.*, 55, 537–551, doi:10.3189/002214309788816678, 2009. 5935
- Picard, G., Domine, F., Krinner, G., Arnaud, L., and Lefebvre, E.: Inhibition of the positive snow-albedo feedback by precipitation in interior Antarctica, *Nature Climate Change*, 2, 795–798, doi:10.1038/nclimate1590, 2012. 5932
- Piepmeyer, J., Bindlish, R., Brown, S., Dinnat, E., Gales, J., Hong, L., Jackson, T., Lagerloef, G., Le Vine, D., de Matthaëis, P., Meissner, T., and Ruf, C.: Aquarius radiometer post-launch calibration for product version 2, Aquarius Project Document: AQ-014-PS-0015, Tech. Rep. AQ-014-PS-0015, NASA and CONAE, 2013. 5928
- Rautiainen, K., Lemmetyinen, J., Pulliainen, J., Vehvilainen, J., Drusch, M., Kontu, A., Kainulainen, J., and Seppanen, J.: L-band Radiometer Observations of Soil Processes in Boreal and Subarctic Environments, *IEEE T. Geosci. Remote*, 50, 1483–1497, doi:10.1109/TGRS.2011.2167755, 2012. 5924, 5940
- Schneider, D. P. and Steig, E. J.: Spatial and temporal variability of Antarctic ice sheet microwave brightness temperatures, *Geophys. Res. Lett.*, 29, 1964, doi:10.1029/2002GL015490, 2002. 5935
- Schneider, D. P., Steig, E. J., and Comiso, J. C.: Recent climate variability in Antarctica from satellite-derived temperature data, *J. Climate*, 17, 1569–1583, doi:10.1175/1520-0442(2004)017<1569:RCVIAF>2.0.CO;2, 2004. 5935
- Surdyk, S.: Using microwave brightness temperature to detect short-term surface air temperature changes in Antarctica: an analytical approach, *Remote Sens. Environ.*, 80, 256–271, 2002. 5923
- Tedesco, M., Abdalati, W., and Zwally, H. J.: Persistent surface snowmelt over Antarctica (1987–2006) from 19.35 GHz brightness temperatures, *Geophys. Res. Lett.*, 34, 18504, doi:10.1029/2007GL031199, 2007. 5932
- Torinesi, O., Fily, M., and Genthon, C.: Variability and trends of the summer melt period of Antarctic ice margins since 1980 from microwave sensors, *J. Climate*, 16, 1047–1060, doi:10.1175/1520-0442(2003)016<1047:VATOTS>2.0.CO;2, 2003. 5932
- Ulaby, F., Moore, R., and Fung, A.: *Microwave Remote Sensing*. 3, Artech house, Norwood, MA, 1986. 5932
- Urbini, S., Frezzotti, M., Gandolfi, S., Vincent, C., Scarchilli, C., Vittuari, L., and Fily, M.: Historical behaviour of Dome C and Talos Dome (East Antarctica) as investigated by

## Aquarius weekly-gridded products to monitor the polar regions

L. Brucker et al.

[Title Page](#)
[Abstract](#)
[Introduction](#)
[Conclusions](#)
[References](#)
[Tables](#)
[Figures](#)
[⏪](#)
[⏩](#)
[◀](#)
[▶](#)
[Back](#)
[Close](#)
[Full Screen / Esc](#)
[Printer-friendly Version](#)
[Interactive Discussion](#)

snow accumulation and ice velocity measurements, *Global Planet. Change*, 60, 576–588, doi:10.1016/j.gloplacha.2007.08.002, 2008. 5936

Utku, C. and Le Vine, D.: Topographic signatures in Aquarius radiometer and scatterometer response, *IEEE T. Geosci Remote*, in press, 14 pp., doi:10.1109/TGRS.2013.2280015, 2013. 5933

Warren, S. G. and Brandt, R. E.: Optical constants of ice from the ultraviolet to the microwave: a revised compilation, *J. Geophys. Res.*, 113, 14220, doi:10.1029/2007JD009744, 2008. 5923

Wentz, F. and Le Vine, D.: Aquarius salinity retrieval algorithm (Version 2) Algorithm Theoretical Basis Document (ATBD), Tech. Rep. 082912, RSS Technical Report, 2012. 5925, 5927, 5928, 5930

Winebrenner, D. P., Arthern, R. J., and Shuman, C. A.: Mapping Greenland accumulation rates using observations of thermal emission at 4.5 cm wavelength, *J. Geophys. Res.*, 106, 33919–33934, doi:10.1029/2001JD900235, 2001. 5932

Yueh, S.: Estimates of Faraday rotation with passive microwave polarimetry for microwave remote sensing of Earth surfaces, *IEEE T. Geosci Remote*, 38, 2434–2438, doi:10.1109/36.868900, 2000. 5926

Zhao, J., Zou, X., and Weng, F.: WindSat radio-frequency interference signature and its identification over greenland and antarctic, *IEEE T. Geosci Remote*, 51, 4830–4839, doi:10.1109/TGRS.2012.2230634, 2013. 5927

Zwally, H. J., Parkinson, C. L., and Comiso, J. C.: Variability of Antarctic Sea Ice and changes in carbon dioxide, *Science*, 220, 1005–1012, doi:10.1126/science.220.4601.1005, 1983. 5923



## TCD

7, 5921–5970, 2013

## Aquarius weekly-gridded products to monitor the polar regions

L. Brucker et al.

[Title Page](#)
[Abstract](#)
[Introduction](#)
[Conclusions](#)
[References](#)
[Tables](#)
[Figures](#)
[◀](#)
[▶](#)
[◀](#)
[▶](#)
[Back](#)
[Close](#)
[Full Screen / Esc](#)
[Printer-friendly Version](#)
[Interactive Discussion](#)

**Table 2.** Beam-dependent characteristics of the Aquarius L-band scatterometer.

Beam	1	2	3
3 dB two-way footprint size along × across track (km × km)	58 × 71	65 × 91	74 × 122
NE $\sigma^0$ (dB)	−29	−26	−24
Scatterometer sensitivity (dB)	0.04	0.06	0.1
Scatterometer stability for 7 days (dB)	0.13	0.13	0.13

## Aquarius weekly-gridded products to monitor the polar regions

L. Brucker et al.

Title Page

Abstract

Introduction

Conclusions

References

Tables

Figures

⏪

⏩

◀

▶

Back

Close

Full Screen / Esc

Printer-friendly Version

Interactive Discussion

**Table 3.** Product names with the list of variables per beams and orbits.

<b>Aquarius 36 km weekly-polar-gridded brightness temperature, and sea surface salinity</b>	
TBV, TBH	
TBV_STD, TBH_STD	Beams 1, 2, and 3
NFP_RAD	Orbits ascending, descending, and combined
SSS, SSS_STD	
ICEF_RAD, ICEF_STD_RAD	
<b>Aquarius 36 km weekly-polar-gridded normalized radar cross section</b>	
NRCS_VV, NRCS_VH, NRCS_HH	
NRCS_VV_STD, NRCS_VH_STD, NRCS_HH_STD	Beams 1, 2, and 3
NFP_SCA	Orbits ascending, and descending
ICEF_SCA, ICEF_STD_SCA	
<b>Aquarius 36 km weekly-polar-gridded sea surface salinity 3 beams (SSS3b)</b>	
SSS3b	
SSS3b_STD	Beams 1, 2, and 3 combined
NFP_SSS3b	Orbits combined
ICEF_SSS3b, ICEF_STD_SSS3b	

## Aquarius weekly-gridded products to monitor the polar regions

L. Brucker et al.

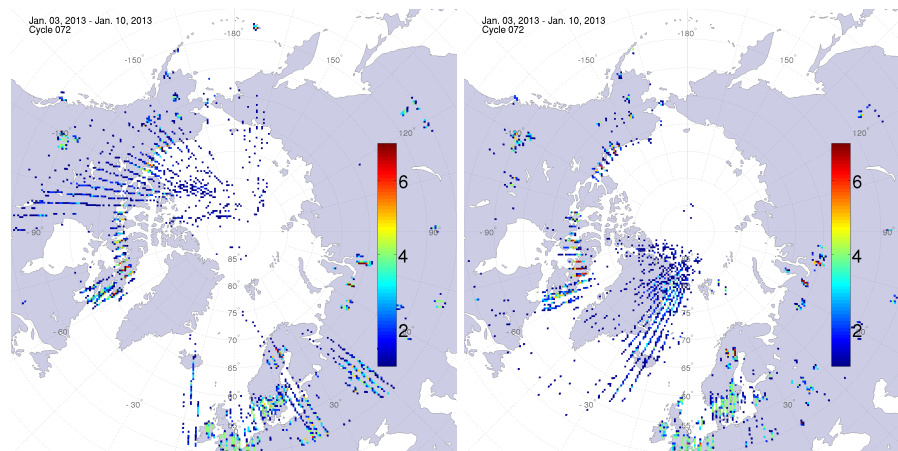


**Fig. 1.** Map of RFI occurrences (i.e. number of footprint with either a moderate or severe RFI contamination) during cycle 72 (3 January–10 January 2013) in the NH for ascending (left) and descending (right) orbits.

[Title Page](#)[Abstract](#)[Introduction](#)[Conclusions](#)[References](#)[Tables](#)[Figures](#)[⏪](#)[⏩](#)[◀](#)[▶](#)[Back](#)[Close](#)[Full Screen / Esc](#)[Printer-friendly Version](#)[Interactive Discussion](#)

## Aquarius weekly-gridded products to monitor the polar regions

L. Brucker et al.

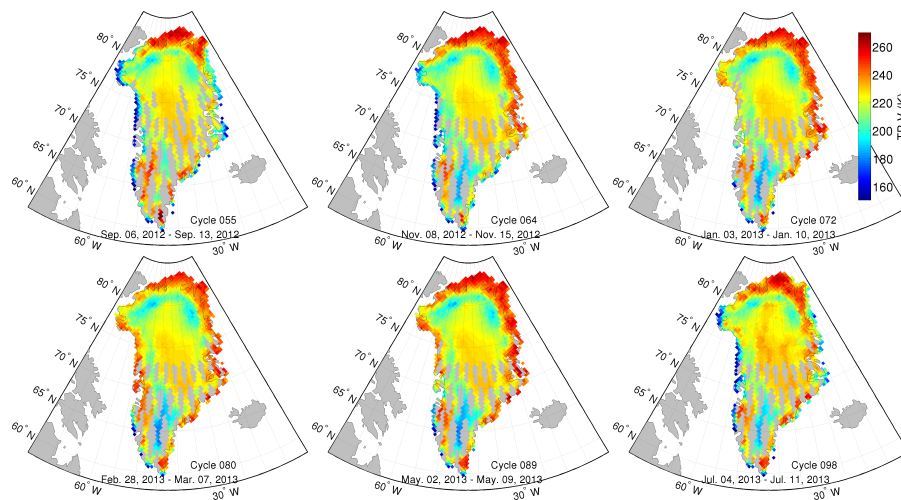


**Fig. 2.** Maps of TB (beam 3) at V polarization (in K) over the GIS for every other month. Grid cells with land fraction less than 0.25 were masked.

[Title Page](#)[Abstract](#)[Introduction](#)[Conclusions](#)[References](#)[Tables](#)[Figures](#)[⏪](#)[⏩](#)[⏴](#)[⏵](#)[Back](#)[Close](#)[Full Screen / Esc](#)[Printer-friendly Version](#)[Interactive Discussion](#)



**Aquarius  
weekly-gridded  
products to monitor  
the polar regions**

L. Brucker et al.

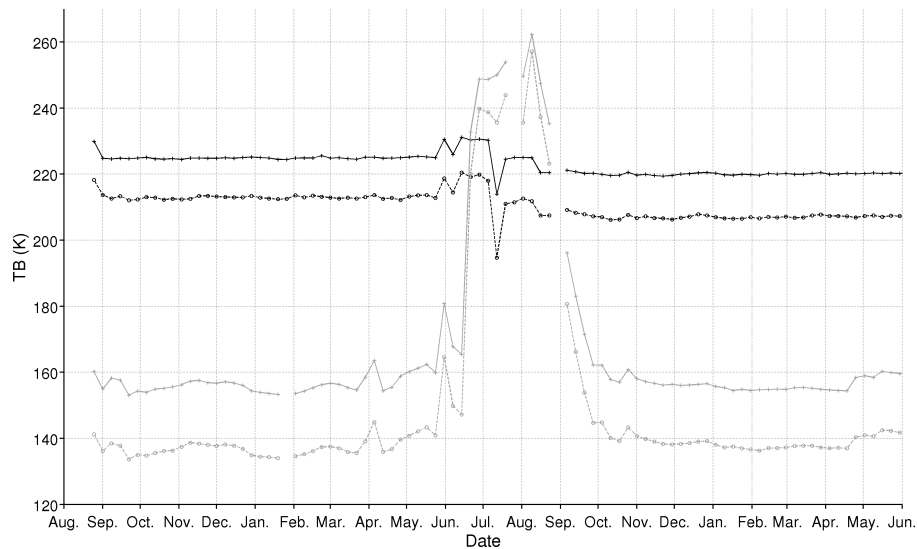


**Fig. 4.** Time series of TB (beam 1) at V (+) and H (o) polarizations near Summit (black), and South Dome (gray).

[Title Page](#)[Abstract](#)[Introduction](#)[Conclusions](#)[References](#)[Tables](#)[Figures](#)[⏪](#)[⏩](#)[◀](#)[▶](#)[Back](#)[Close](#)[Full Screen / Esc](#)[Printer-friendly Version](#)[Interactive Discussion](#)

## Aquarius weekly-gridded products to monitor the polar regions

L. Brucker et al.

Title Page

Abstract

Introduction

Conclusions

References

Tables

Figures

⏪

⏩

◀

▶

Back

Close

Full Screen / Esc

Printer-friendly Version

Interactive Discussion

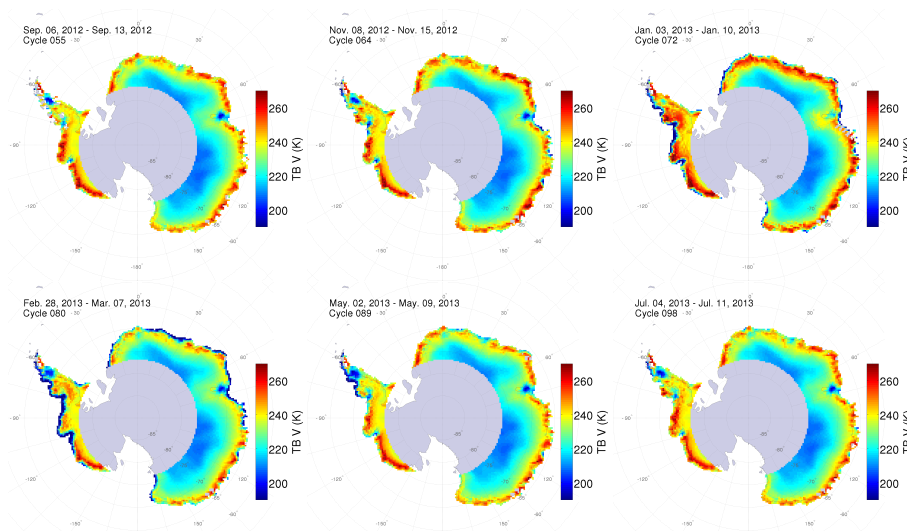


**Fig. 5.** Maps of TB (beam 3) at V polarization (in K) over the AIS for every other month. Grid cells with land fraction less than 0.25 were masked.





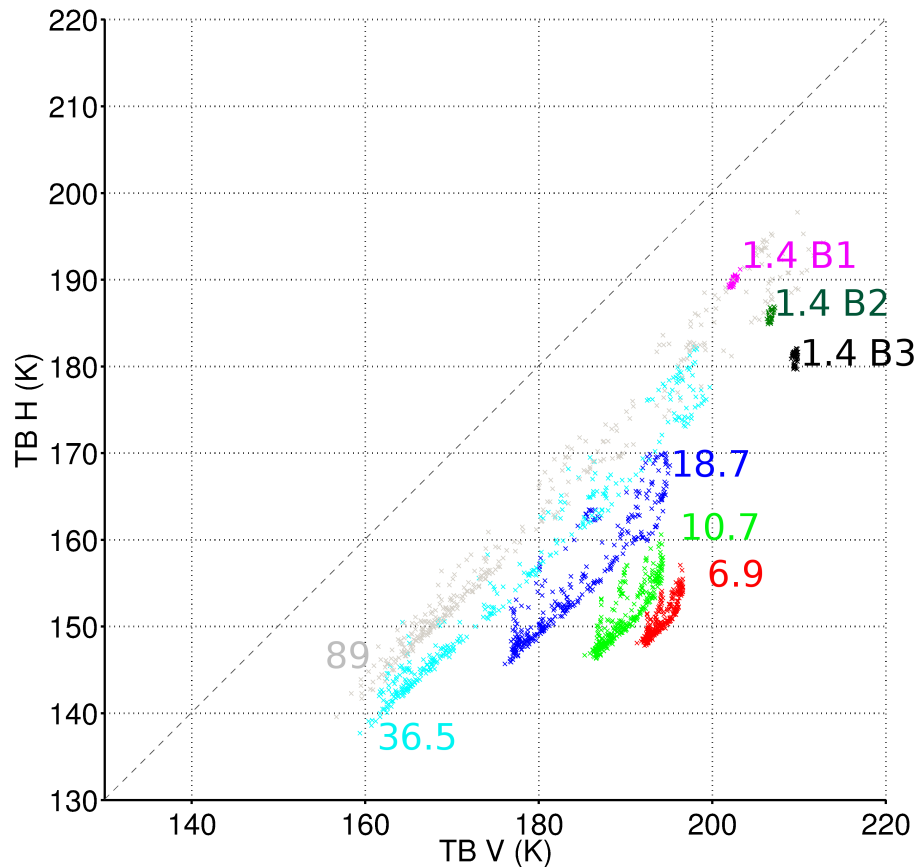


**Fig. 8.** TB H as a function of TB V at Dome C, Antarctica, using one year of data. 2012 Aquarius TBs and 2010 AMSR2 TBs were used providing 1.413 GHz data at three different incidence angles, and 6.9, 10.7, 18.7, 36.5, and 89 GHz data, respectively.

## Aquarius weekly-gridded products to monitor the polar regions

L. Brucker et al.

Title Page

Abstract

Introduction

Conclusions

References

Tables

Figures

⏪

⏩

◀

▶

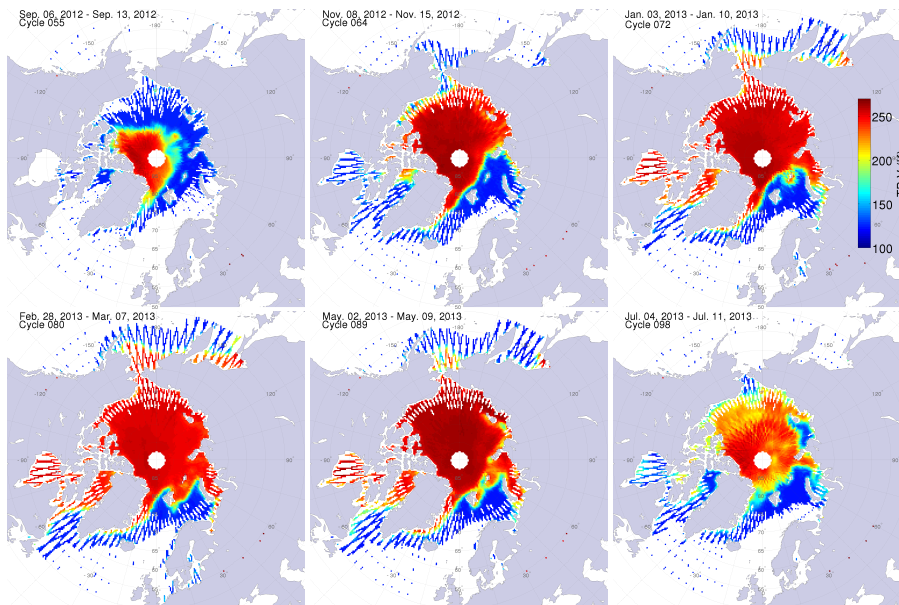
Back

Close

Full Screen / Esc

Printer-friendly Version

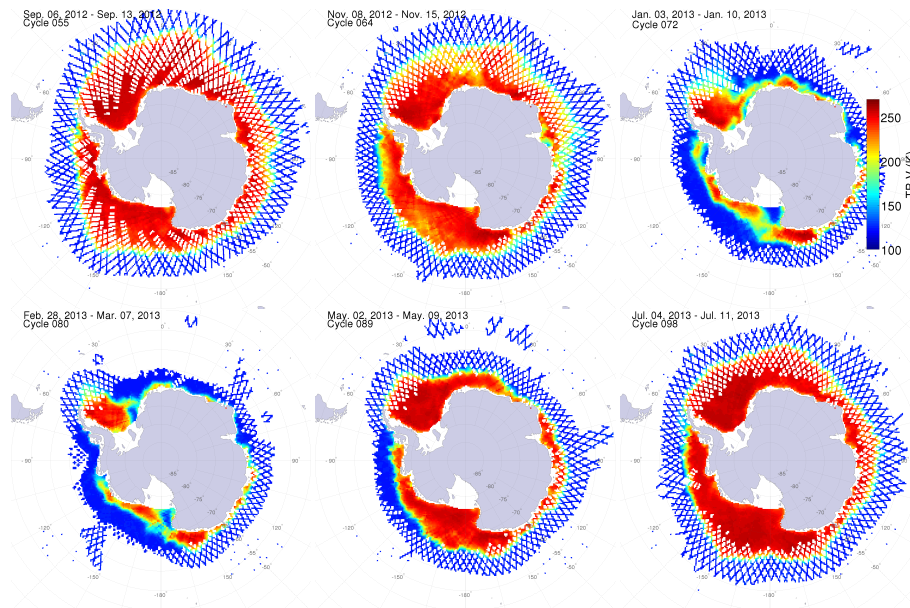
Interactive Discussion



**Fig. 9.** Maps of TB (beam 3) at V polarization over the NH sea ice for every other month. Grid cells where the land fraction was more than 0.25 were masked.

## Aquarius weekly-gridded products to monitor the polar regions

L. Brucker et al.

[Title Page](#)[Abstract](#)[Introduction](#)[Conclusions](#)[References](#)[Tables](#)[Figures](#)[⏪](#)[⏩](#)[◀](#)[▶](#)[Back](#)[Close](#)[Full Screen / Esc](#)[Printer-friendly Version](#)[Interactive Discussion](#)

**Fig. 10.** Maps of TB (beam 3) at V polarization over the SH sea ice for every other month. Grid cells where the land fraction was more than 0.25 were masked.



## Aquarius weekly-gridded products to monitor the polar regions

L. Brucker et al.

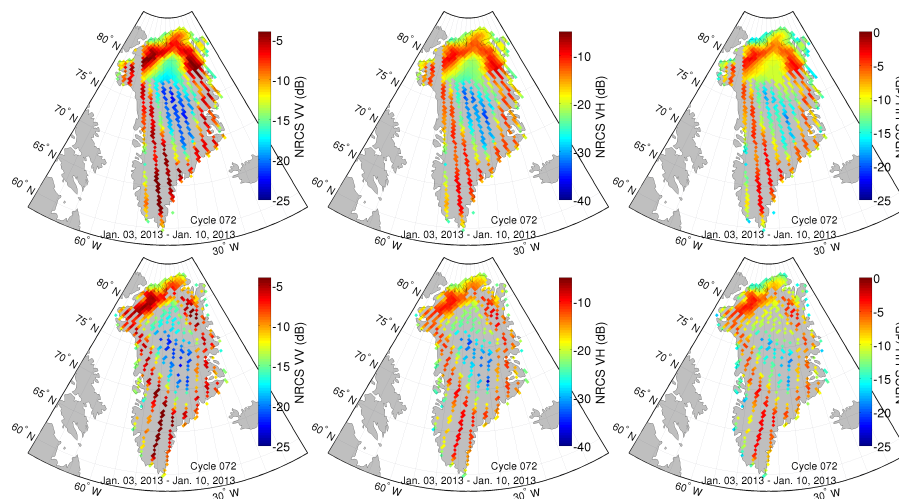


**Fig. 12.** NRCS (beam 3) at VV (left panels), VH (middle panels), and at HH (right panels) polarizations recorded over the GIS during the cycle 72 (3–10 January 2013) and during ascending orbits (first row), and descending orbits (second row). Grid cells where the land fraction was less than 0.25 were masked.

[Title Page](#)[Abstract](#)[Introduction](#)[Conclusions](#)[References](#)[Tables](#)[Figures](#)[◀](#)[▶](#)[◀](#)[▶](#)[Back](#)[Close](#)[Full Screen / Esc](#)[Printer-friendly Version](#)[Interactive Discussion](#)

## Aquarius weekly-gridded products to monitor the polar regions

L. Brucker et al.

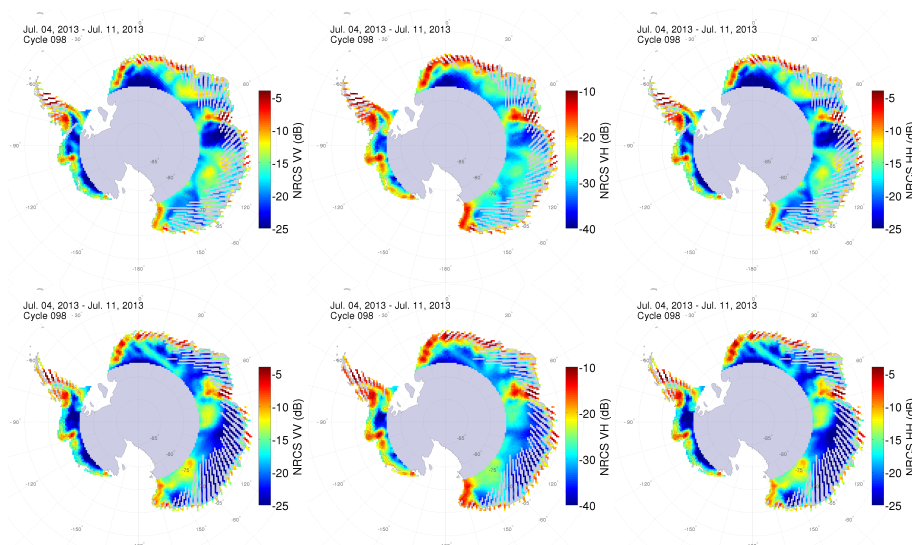


**Fig. 13.** NRCS (beam 3) at VV (left panels), VH (middle panels), and at HH (right panels) polarizations recorded over the AIS during the cycle 98 (4–11 July 2013) and during ascending orbits (first row), and descending orbits (second row). Grid cells where the land fraction was less than 0.25 were masked.

Title Page

Abstract

Introduction

Conclusions

References

Tables

Figures

◀

▶

◀

▶

Back

Close

Full Screen / Esc

Printer-friendly Version

Interactive Discussion

## Aquarius weekly-gridded products to monitor the polar regions

L. Brucker et al.

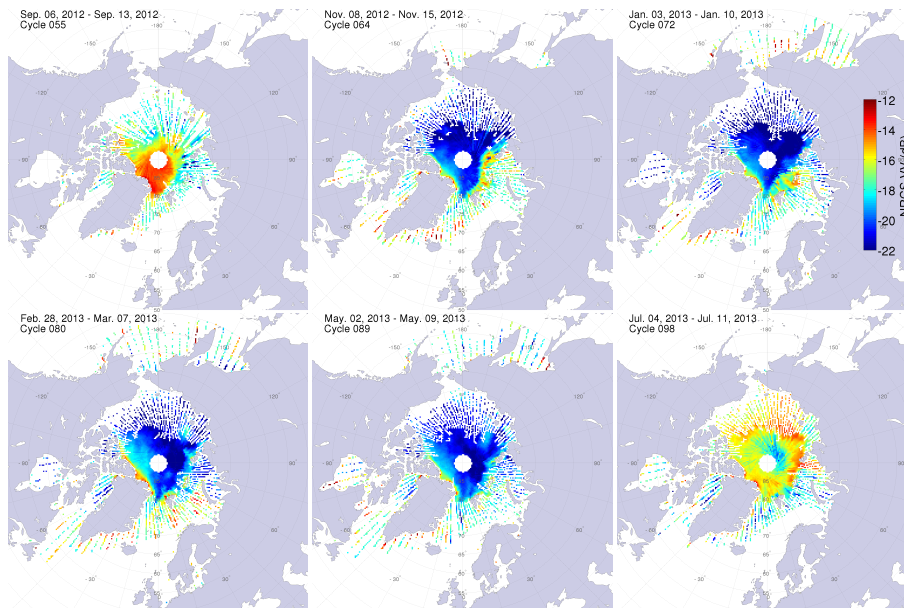


**Fig. 14.** Maps of beam 3 NRCS VV observed during ascending orbits over the NH sea ice for every other month. Grid cells where the land fraction was more than 0.25 were masked.

Title Page

Abstract

Introduction

Conclusions

References

Tables

Figures

⏪

⏩

◀

▶

Back

Close

Full Screen / Esc

Printer-friendly Version

Interactive Discussion

## Aquarius weekly-gridded products to monitor the polar regions

L. Brucker et al.

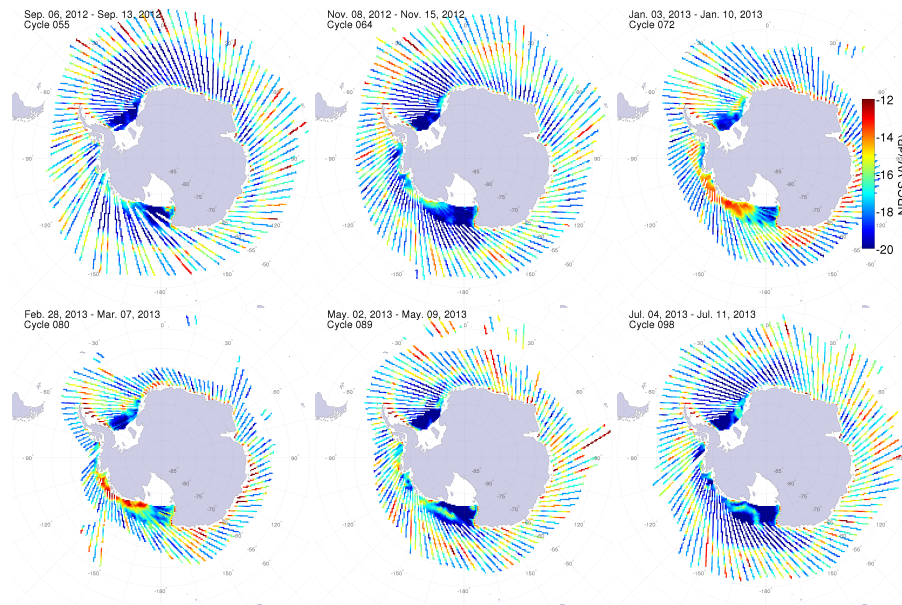


**Fig. 15.** Maps of beam 3 NRCS VV observed during ascending orbits over the SH sea ice for every other month. Grid cells where the land fraction was more than 0.25 were masked.

[Title Page](#)[Abstract](#)[Introduction](#)[Conclusions](#)[References](#)[Tables](#)[Figures](#)[⏪](#)[⏩](#)[◀](#)[▶](#)[Back](#)[Close](#)[Full Screen / Esc](#)[Printer-friendly Version](#)[Interactive Discussion](#)

## Aquarius weekly-gridded products to monitor the polar regions

L. Brucker et al.

Title Page

Abstract

Introduction

Conclusions

References

Tables

Figures

◀

▶

◀

▶

Back

Close

Full Screen / Esc

Printer-friendly Version

Interactive Discussion

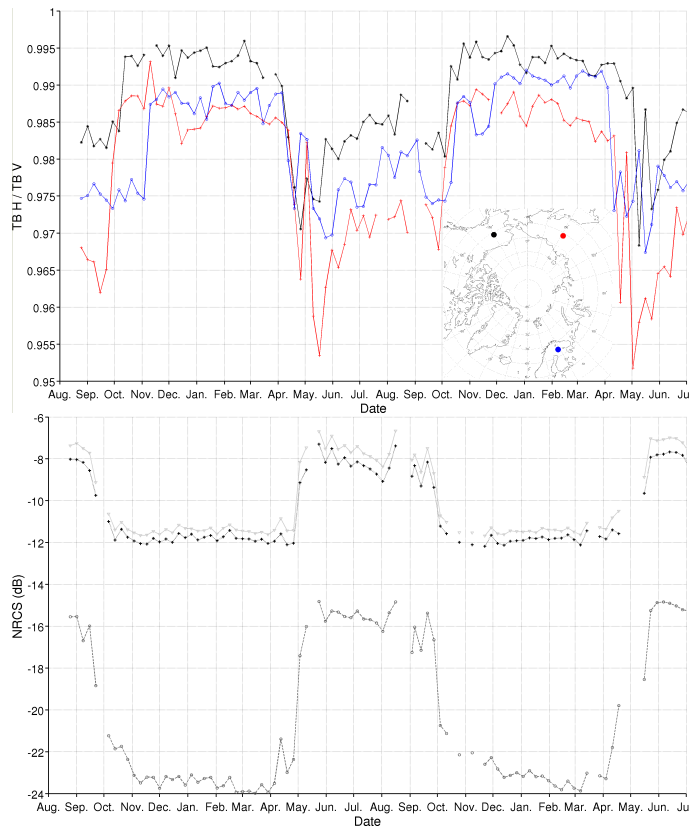


**Fig. 16.** (Top) time series of the TB H/V ratio in three locations Northern America (Alaska)  $66^{\circ}$  N,  $150^{\circ}$  W (black \*), Northern Europe (Finland)  $67.5^{\circ}$  N,  $29^{\circ}$  E (blue o), and Asia (Russia)  $66^{\circ}$  N,  $149.5^{\circ}$  E (red +). (Bottom) time series NRCS at VV (plus symbols), VH (circles), and HH (downward triangles) for the location in Asia.



## Aquarius weekly-gridded products to monitor the polar regions

L. Brucker et al.

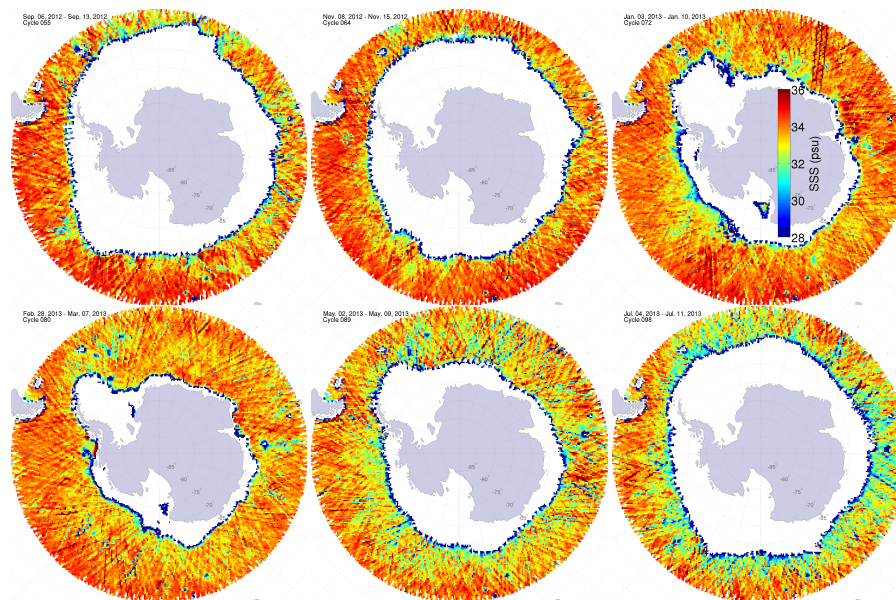


**Fig. 18.** Maps of SSS3b over the SH high latitudes for cycles every other month. Grid cells where the land fraction was more than 0.25 were masked.

[Title Page](#)[Abstract](#)[Introduction](#)[Conclusions](#)[References](#)[Tables](#)[Figures](#)[◀](#)[▶](#)[◀](#)[▶](#)[Back](#)[Close](#)[Full Screen / Esc](#)[Printer-friendly Version](#)[Interactive Discussion](#)